The Astrophysical Journal, 883:74 (16pp), 2019 September 20 https://doi.org/10.3847/1538-4357/ab3c50

Forward Modeling of a Pseudostreamer

Nishu Karna[1], Antonia Savcheva[1], Kévin Dalmasse[2], Sarah Gibson[3], Svetlin Tassev[1], Giuliana de Toma[3], and Edward E. DeLuca[1]

[1] Harvard-Smithsonian Center for Astrophysics, 60 Garden Street, Cambridge, MA 02138, USA; nishu.karna@cfa.harvard.edu

[2] IRAP, Université de Toulouse, CNRS, CNES, UPS, F-31028 Toulouse, France

[3] High Altitude Observatory, 3300 Center Green Drive, Boulder, CO, USA

Received 2018 October 2; revised 2019 August 14; accepted 2019 August 15; published 2019 September 23

Abstract

In this paper, we present an analysis of a pseudostreamer embedding a filament cavity, observed on 2015 April 18 on the solar southwest limb. We use the flux-rope insertion method to construct nonlinear force-free field (NLFFF) models constrained by observed *Solar Dynamics Observatory* (*SDO*)/AIA coronal structures and the *SDO*/Helioseismic Magnetic Imager photospheric magnetogram. The resulting magnetic field models are forward-modeled to produce synthetic data directly comparable to Mauna Loa Solar Observatory/Coronal Multichannel Polarimeter (CoMP) observations of the intensity and linear polarization of the Fe XIII 1074.7 nm infrared coronal emission line using FORWARD. In addition, we determine the location of quasi-separatrix layers in the magnetic models, producing a Q-map from which the signatures of magnetic null points and separatrices can be identified. An apparent magnetic null observed in linear polarization by CoMP is reproduced by the model and appears in the region of the 2D-projected magnetic null in the Q-map. Further, we find that the height of the CoMP null is better reproduced by our NLFFF model than by the synthetic data we produce with potential-field source-surface models, implying the presence of a flux rope in the northern lobe of the pseudostreamer.

Key words: Sun: corona – Sun: filaments, prominences – Sun: magnetic fields

1. Introduction

Determining the topological skeleton of the coronal magnetic field is of high importance. One key topological structure is a pseudostreamer, which is also known as a unipolar streamer as it separates coronal holes of the same polarity (Hundhausen 1972; Zhao & Webb 2003; Wang et al. 2007b; Titov et al. 2012). This distinguishes pseudostreamers from helmet streamers, which separates an open field of opposite polarities. Pseudostreamers overlie two (or an even number of) polarity inversion lines (PILs) when viewed in 2D projection at the limb. In the lower corona, the field lines are closed, and above the closed field, two domains of the open field of the same polarity come together to form the spine of the pseudostreamer (Rachmeler et al. 2014). Simple (double-PIL) pseudostreamers in a 2D cross section possess a single X-point or a magnetic null point observed above the limb (Priest 2014). Pseudostreamer-like structures show a wide spectrum of scales. Their base and null-point height can vary from less than 100 Mm up to 700 Mm (Wang et al. 2007a, 2007b; Velli et al. 2011). The detection of magnetic nulls helps to identify the critical points in the coronal field that facilitate solar eruptions (Gibson et al. 2017). Therefore, it is important to study pseudostreamer magnetic configurations. As in Gibson et al. (2017), we note that the two-dimensional interpretation of a magnetic null does not differentiate between a true three-dimensional magnetic null point and topological structure such as multiple null points along a line, a magnetic separator, or a hyperbolic flux tube (see, e.g., Titov et al. 2002, 2011; Aulanier et al. 2005; Parnell et al. 2010).

In the corona, the high plasma temperature broadens the line profile by orders of magnitudes above the Zeeman splitting. Also, the line-of-sight (LoS) integration complicates the interpretation of optically thin coronal line measurements, making direct measurements of the magnetic field in the corona difficult (Wiegelmann et al. 2006). Recent analyses have demonstrated the usefulness of coronal linear-polarization measurements for diagnosing coronal magnetic topology (Dove et al. 2011; Bąk-Stęślicka et al. 2013; Rachmeler et al. 2013; Gibson et al. 2017). However, measurements of coronal circular polarization—proportional to the LoS magnetic field strength—remain rare (Lin et al. 2004). Therefore, we rely on magnetic field models constrained by the photospheric magnetic field measurements (Mackay & Yeates 2012).

In this paper, we analyze a pseudostreamer as observed in extreme ultraviolet (EUV) intensity by the *Solar Dynamics Observatory* (*SDO*)/Atmospheric Imaging Assembly (AIA) and in infrared (IR) linear polarization from Coronal Multichannel Polarimeter (CoMP). This pseudostreamer was the subject of a recent paper which found that a potential-field extrapolation of the photospheric field (containing no currents) resulted in an apparent magnetic null height that was too low and magnetic flux expansion that was too small, in comparison to linear-polarization measurements of the pseudostreamer (Gibson et al. 2017). This motivates the current work, in which we develop nonlinear force-free field (NLFFF) models—with currents included—to more accurately model the pseudostreamer's 3D magnetic structure.

There are several methods for numerically computing NLFFFs, such as the magnetofrictional (MF) method (van Ballegooijen 2004; Valori et al. 2005, 2007; Mackay et al. 2011; Cheung & DeRosa 2012; Gibb et al. 2014), the Grad–Rubin method (Grad & Rubin 1958; Sakurai 1981; Amari et al. 1999, 2006; Wheatland 2004, 2006; Malanushenko et al. 2012), the optimization approach (Wheatland et al. 2000; Wiegelmann 2004; Wiegelmann et al. 2007), the MHD relaxation method (Chodura & Schlueter 1981; Yang et al. 1986; Mikic & McClymont 1994; Roumeliotis 1996; Inoue et al. 2011, 2012; Jiang et al. 2011; Jiang & Feng 2012), or the boundary-element method (Yan & Sakurai 2000; Yan & Li 2006; He & Wang 2008; He et al. 2011). We use the van

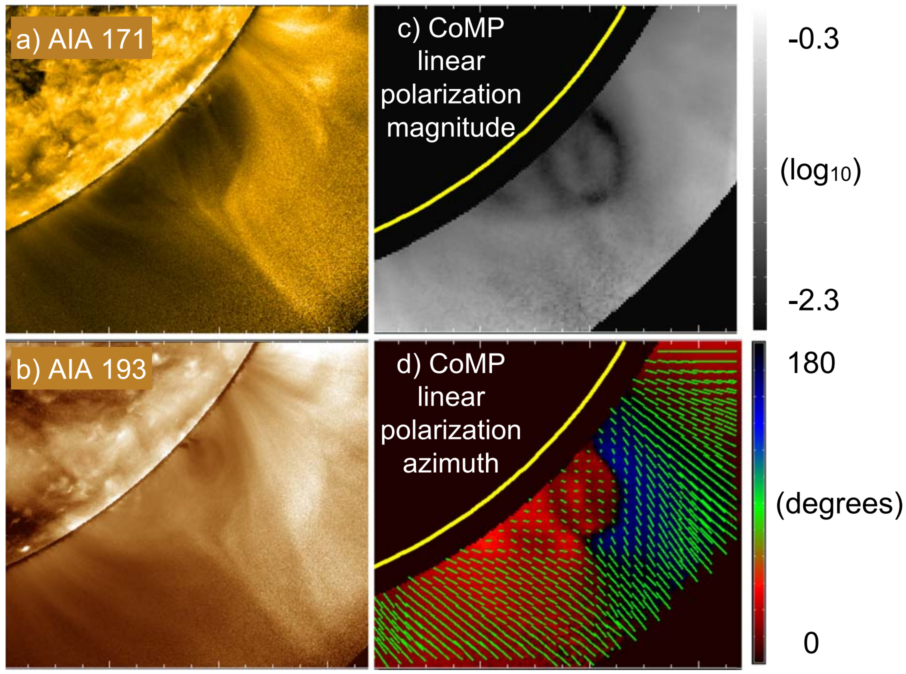

Figure 1. (a) AIA 171 Å and (b) AIA 193 Å intensity (19:30 UT, 2015 April 18). (c) CoMP linear-polarization magnitude (L/I) and (d) azimuth = 0.5 tan (U/Q) (150 image average; 18:43–19:58 UT). Azimuth direction is indicated by green vectors and by color table (black = radial; blue = clockwise tilt; red = counterclockwise tilt). The solar photosphere is indicated by the yellow curves in (c) and (d). Figure reproduced from Gibson et al. (2017).

Ballegooijen (2004) flux-rope insertion method to perform the NLFFF modeling here. This approach allows the direct incorporation of observations of structures seen in the chromosphere (filament) and corona (cavity) to appropriately model coronal currents in the form of an inserted flux rope based on LoS photospheric magnetograms.

This paper is organized as follows. In Section 2, we present the observations and previous studies of the pseudostreamer. In Section 3, we present a brief description of the magnetic model, the initial magnetic field configuration, the flux-rope insertion method, and the MF relaxation method. In Section 4, we present the details of the QSL calculation. In Section 5, we present synthetic pseudostreamer observations forward modeled from the NLFFF model, and compare them. to observations. We conclude with a summary of our findings in Section 6.

2. Observations and Previous Studies

The pseudostreamer was observed from 2015 April 17 to 19 on the southwest limb. On August 18, observations from the AIA (Lemen et al. 2012) on board the *SDO* (Pesnell et al. 2012) clearly show the two lobes of the pseudostreamer and a prominence and cavity evident only in the northern lobe (Figures 1 (a)–(b)). The cavity in the northern lobe erupted as a narrow CME on April 19, as observed by AIA and SWAP. Observations from the Heliospheric Magnetic Imager (HMI) on board *SDO* (Hoeksema et al. 2014) showed that the pseudostreamer was bounded by two negative polarity magnetic fields and was centered above a positive polarity field. Figures 1(c)–(d) show linear-polarization measurements in the Fe XIII coronal emission line at 1074.7 nm by the Mauna Loa Solar Observatory CoMP telescope (Tomczyk et al. 2008).

Linear polarization is sensitive to plane-of-sky (PoS) magnetic field direction, and the azimuth angle (Figure 1(d)) is an LoS intensity-weighted average of this angle. A 90° rotation of the azimuth angle occurs when the local magnetic vector crosses the van Vleck angle of $\vartheta_B = 54\overset{\circ}{.}74$. Thus, the azimuth is either parallel or perpendicular to the (intensity-weighted) PoS magnetic field angle. Linear-polarization magnitude diminishes to zero at the van Vleck angle, resulting in dark structures as seen in Figure 1(c). Indeed, the lobe-like structures shown in Figure 1 are expected for a pseudostreamer magnetic structure, with an apparent magnetic null identifiable as the intersection of the dark lobes as shown in an analytical simulation by Rachmeler et al. (2014).

Gibson et al. (2017) demonstrated that the linear-polarization azimuth represented a new means of calculating the nonradial expansion of the magnetic flux tube, independent of any assumed coronal field model. We will discuss this further in Section 5. The observed CoMP linear-polarization expansion factor was shown to be significantly larger than the expansion predicted by a forward modeled potential-field extrapolation (Gibson et al. 2017). Moreover, the apparent magnetic null observed by CoMP was higher than that of the potential field. The authors argued that the prominence cavity in the northern pseudostreamer lobe indicated the presence of currents, perhaps in the form of a flux rope, that could not be captured by the potential-field model.

3. NLFFF Modeling

3.1. Flux-rope Insertion Method

In the corona, the magnetic pressure is generally much larger than the gas pressure, i.e., the corona is a low-β environment, which can be assumed is nearly force free, or $\boldsymbol{j} \times \boldsymbol{B} = 0$, where $\boldsymbol{B}(\boldsymbol{r})$ is the magnetic field and $\boldsymbol{j}(\boldsymbol{r})$ is the electric current density. This implies $\nabla \times \boldsymbol{B} = \alpha\boldsymbol{B}$, where $\alpha(\boldsymbol{r})$ is the torsion parameter. When $\alpha(\boldsymbol{r}) = 0$, we have a potential field; if $\alpha(\boldsymbol{r})$ is constant, we have a linear force-free field (LFFF); and when $\alpha(\boldsymbol{r})$ varies among different field lines and is constant along any particular field line, it is an NLFFF. NLFFFs are the most realistic coronal fields, i.e., representative of observed coronal structures, but are the most challenging to compute.

In this paper, we use the van Ballegooijen (2004) flux-rope insertion method for calculating NLFFF models to understand the magnetic structures of the pseudostreamer. The method involves inserting a magnetic flux rope into a potential field (van Ballegooijen 2004; Bobra et al. 2008; Savcheva & van Ballegooijen 2009; Su et al. 2009, 2011; Savcheva et al. 2012, 2016). In the model, the filament is represented by a helical flux rope, and the flux rope is overlaid by a coronal arcade, preventing it from rising outward. The arcade is approximated using potential-field modeling (van Ballegooijen 2004).

This method has been successfully used by Bobra et al. (2008), Su et al. (2011), and Asgari-Targhi & van Ballegooijen (2012) to study active regions with filaments; by Savcheva & van Ballegooijen (2009) and Savcheva et al. (2012, 2016) to study the evolution of soft X-ray sigmoids; and by Su & van Ballegooijen (2012) to study quiescent prominence cavities. In this paper, we use it to study for the first time the magnetic structure of a pseudostreamer.

We utilize the Coronal Modeling System (CMS) to model nonpotential magnetic fields in the solar corona, which implements the insertion of flux ropes. The flux-rope insertion method reconstructs the magnetic field in the solar corona using LoS photospheric magnetograms, because the LoS component of the photospheric fields is measured with much greater precision in quiet-Sun areas than the transverse fields and are not subject to the 180° ambiguity problem (Bobra et al. 2008). They are suitable for modeling quiescent filaments as in the case being studied in this paper.

First, a wedge-shaped high-resolution model domain covering a large area surrounding the region of interest (RoI) is selected. In the RoI, the lower boundary condition is a high-resolution HMI LoS magnetogram. The top boundary is at the "source surface," where the magnetic field is assumed to be radial and open. The magnetic field $\boldsymbol{B}(\boldsymbol{r})$ is described in terms of the vector potential ($\boldsymbol{B} = \nabla \times \boldsymbol{A}$), so that the solenoidal condition, $\nabla \cdot \boldsymbol{B} = 0$, is satisfied automatically. The vector potential is further modified to create a "cavity" of zero field in the region above the selected path, following the observed filament. Then, the flux rope is inserted into this cavity as a combination of axial and poloidal flux. The vector potential is modified again, with the axial flux represented by a thin tube that runs horizontally along the length of the selected path. The poloidal flux is inserted as a set of closed field lines that wrap around the tube. The flux rope connects to the photosphere at the two ends of the path via two short vertical sections. The net flux in each end is subtracted from the inserted axial flux so that the radial fluxes in these vertical sections counteract the additional sources initially added to the magnetogram. This ensures that the original flux distribution in the LoS magnetogram is recovered after the flux rope is inserted. (van Ballegooijen 2004; Bobra et al. 2008).

A set (or a grid) of models are constructed with different combinations of axial flux, Φ_{axi}, and poloidal flux, F_{pol}. These field configurations are not in force-free equilibrium. MF relaxation is then applied to drive the magnetic field toward a force-free state. MF relaxation expands the flux rope until its magnetic pressure balances the magnetic tension from the surrounding potential arcade. The method iterates the following induction equation (in the absence of any plasma equations):

$$\frac{\partial \boldsymbol{A}}{\partial t} = \boldsymbol{v} \times \boldsymbol{B} - \eta_i \nabla \times \boldsymbol{B} + \frac{\boldsymbol{B}}{B^2} \nabla \cdot (\eta_4 B^2 \nabla \alpha) \tag{1}$$

where η_i is the ordinary diffusion and η_4 is the hyperdiffusion (Boozer 1986; Bhattacharjee & Hameiri 1986), and both are constant in space. η_4 acts to smooth gradients in α in the direction across field lines by suppressing numerical artifacts while preserving helicity. α is the magnetic torsion parameter defined by $\alpha \equiv \boldsymbol{j} \cdot (\boldsymbol{B}/B^2)$. The current $\boldsymbol{j} = \nabla \times \boldsymbol{B}$ and $\boldsymbol{v}$ is the MF velocity, given by

$$\boldsymbol{v} = (f\boldsymbol{j} - v_1 \hat{r} \times \boldsymbol{B}) \times \frac{\boldsymbol{B}}{B^2}, \tag{2}$$

where f is the coefficient of magnetofriction and v_1 describes the effects of buoyancy and pressure gradients in the photosphere, which is applied to effectively float the current and not allow any j_z to pass through the lower boundary and leave it unchanged (Bobra et al. 2008, Appendix A). The MF method assumes plasma velocity to be proportional to the Lorentz force, so that the field evolves toward a nonlinear force-free state.

During the relaxation process, the bottom boundary is fixed as defined by the LoS magnetogram, the side boundaries are fixed as defined by the potential-field values of the low-resolution full-Sun potential-field extrapolation, and the top boundary is open. Other than the fixed boundaries, magnetic fields are allowed to vary throughout the wedge volume.

3.2. Application to the 2015 April 18 Pseudostreamer

The pseudostreamer structure was observed on the western limb. Therefore, we had to use magnetograms that were taken several days earlier. This is a reasonable approximation for polar crown cavities as they have been statistically observed to stay stable over many days and weeks (Karna et al. 2015). We combined four full-disk HMI photospheric overlapping LoS magnetograms taken on 2015 April 13–16 (each at 17:01 UT, 24 hr cadence) by the HMI instrument on the *SDO* satellite (Hoeksema et al. (2014) to construct a high-resolution map of the radial component $\boldsymbol{B}(\boldsymbol{r})$ of the magnetic field as a function of longitude and latitude. This served as the lower boundary of the RoI. By rotating the B_z of the April 13 magnetogram to the location of the April 16 magnetogram, we mitigate limb-projection effects.

The observed pseudostreamer extended around 30° in latitude, and the underlying filament extended more than 30° in longitude. Because the model needed to include the overlying coronal fields, we performed global potential-field extrapolations of the photospheric magnetic field in large wedge-shaped high-resolution computational domains surrounding the filament, up to two different choices of source-surface height: (a) 2.5 and (b) 2.8 R_{Sun} from the photosphere. We also left the side boundary conditions of our RoI open for all the NLFFF models. The side boundary conditions on the PFSS models were done in two ways: (1) open as in the NLFFF case and (2) embedded within an extrapolation of the global HMI synoptic map. We will discuss this in detail in Section 5.3.

The flux rope was inserted 14 Mm above the photosphere. We ran two distinct cases: first, inserting one flux rope in the cavity contained in the northern lobe of the pseudostreamer

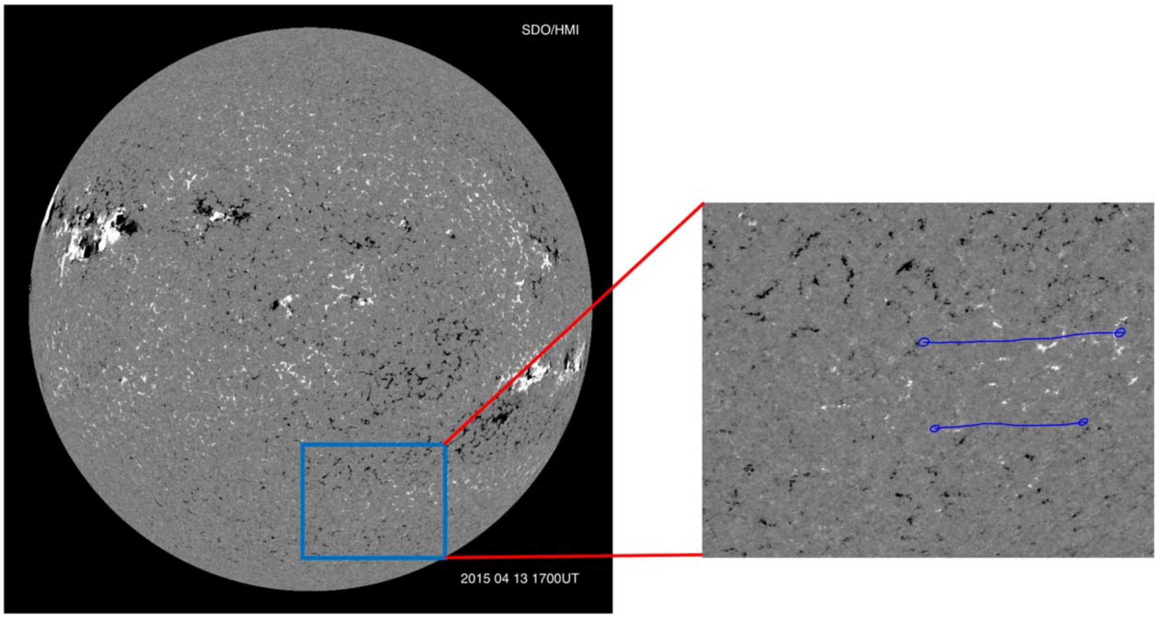

Figure 2. Left: full-disk HMI magnetogram for 2015 April 13, 17:00 UT. The blue rectangular box encloses our region of interest. Right: zoom-in region of interest with selected paths of the north flux rope (NFR) and south flux rope (SFR; blue lines), overlaid on the HMI magnetogram. The two circles at the end of both paths represent where the axial flux of the flux rope is anchored in the photosphere. White and black are positive and negative polarities. The length of the NFR and SFR are 223 Mm and 196 Mm, respectively, where the curvature of the Sun is taken into account in the measurement of the path length.

(Figure 1(b); which we refer to as the north flux rope (NFR)), and second, inserting flux ropes into both lobes of the pseudostreamer (so, both the NFR and an additional south flux rope (SFR)). We started each PIL path in a region of positive polarity and followed the observed polarity line, ending in a region with negative polarity on the opposite side of the PIL. Figure 2 shows the selected paths (NFR and SFR) for April 18, 17:00 UT, overlaid on the HMI magnetogram. The two circles at the end of both paths represent where the flux ropes were anchored in the photosphere. The NFR path was determined by following the path of an observed filament that appeared dark in EUV images from AIA 171 Å on 2015 April 11. The northern filament barbs appeared left-bearing in AIA absorption, so we designed the inserted flux rope similarly to have sinistral orientation and thus be a positive helicity right-handed flux rope. Because no filament was observed in the southern PIL, we considered both signs of helicity for completeness as depicted in the schematic in Figure 3 for the three configurations we modeled. Our expectation was that the same sign of helicity would work best because the hemispheric helicity rule gets stronger with increasing latitude (Pevtsov et al. 2003). The three configurations we modeled are given below:

1. Inserting only one flux rope (1FR), NFR (Figure 3(a)): the path of the flux rope is inserted from the limb to the disk (sinistral orientation, positive helicity). We call this the regular path.
2. Inserting both NFR and SFR (2FR): the path of the SFR runs in the same direction as that of the NFR (Figure 3(b)). Both flux ropes are on the regular path. Both negative and positive poloidal fluxes were tested.
3. Inserting both NFR and SFR (2FR): the path of the SFR is reversed versus the NFR, i.e., the SFR path direction runs from the disk to the limb. We call this the reversed path (Figure 3(c)). Both negative and positive poloidal fluxes were tested.

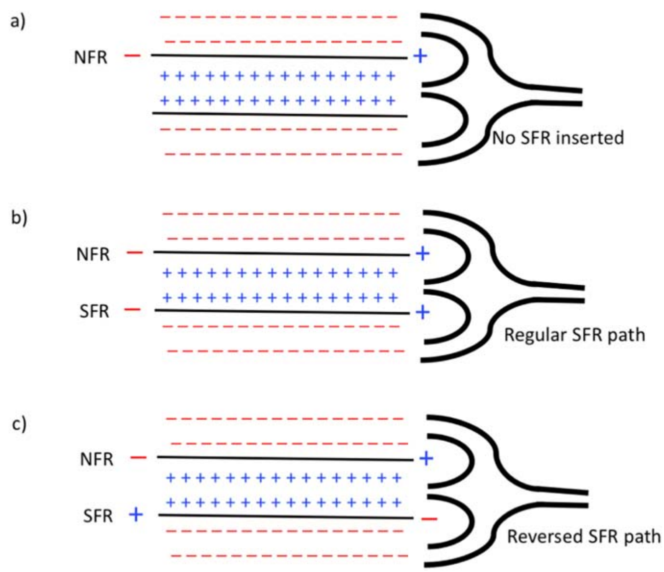

Figure 3. Sketch of the inserted flux-rope paths. (a) Only the NFR is inserted, with axial flux direction from limb to the disk. (b) Both NFR and SFR are inserted, with the same direction of axial flux (limb to disk). (c) The axial flux direction of the SFR is reversed relative to the NFR (disk to limb).

We constructed a set of models with different choices of axial flux, Φ_{axi}, poloidal flux, F_{pol}, and flux-rope heights for all three configurations, which were relaxed to force-free equilibria following the relaxation scheme of Savcheva et al. (2016). During that process, we did not use any ordinary diffusion and kept hyperdiffusion as small as possible so that the inserted poloidal flux was preserved during the relaxation process. The induction equation was iterated until the MF velocity vanished, indicating that the configuration had reached equilibrium; these represented stable NLFFF solutions. In general, either the field approached a nonlinear force-free state, or the field expanded indefinitely toward an open state where axial/poloidal fields were large (Bobra et al. 2008). With each iteration number, the magnetic energy always decreased.

In unstable models, the magnetic free energy decreased more quickly due to "reconnection" (change in connectivity of the field lines), while if the model was stable, then magnetic free energy decreased slowly and asymptotically converged to the energy of the force-free state.

The end result of the relaxation runs was a set of 3D NLFFF models of the magnetic field $\boldsymbol{B}(\boldsymbol{r})$ with a magnetic flux rope located at the location of the observed filament. We tested paths with different lengths and determined that the lengths of the paths had a noticeable effect on the stability along the FRs and even the existence of the pseudostreamer topology, as such a topology did not form for all path lengths. We also tested sensitivity to the flux-rope height parameter by inserting flux ropes at different heights. Similar to our length analysis, we found that the height had a significant effect on the FR's stability.

3.3. NLFFF Results

We ran a grid of 153 different initial sets of parameters in total (both with one and two FRs), with different combinations of axial and poloidal fluxes, ranging from (0.01–5) $\times 10^{21}$ Mx and (0–5) $\times 10^{10}$ Mx cm^{-1}, respectively. The range in axial and poloidal fluxes and flux-rope initial heights are appropriate for the general properties of the observed structure. To enhance the stability of the flux rope, we added two magnetic sources with fluxes of $\pm 1 \times 10^{20}$ Mx to the $\boldsymbol{B}(\boldsymbol{r})$ map at the two ends of the filament's path in both cases (1FR, 2FR) before the flux-rope insertion process as performed in Su & van Ballegooijen (2012). These external sources permanently modify the flux distribution at the footpoints of the filament. The external flux in each end is subtracted from the inserted axial flux so that the radial fluxes counteract the additional sources initially added to the magnetogram and recover the flux distribution (modified by the external magnetic sources) after the flux rope is inserted, as in the original flux-rope insertion methodology. We qualitatively fit to AIA images by overlying the pseudostreamer on top of the AIA images with both one and two flux ropes. Best-fit models (one flux rope and two flux ropes) were selected from the stable models by comparing the location and height of the filaments, size of cavity, and overlying closed and open magnetic field lines to AIA images. We found that the 1FR (NFR) model with axial flux 4×10^{19} Mx and poloidal flux 8×10^{9} Mx cm^{-1} was the best-fit stable model (Model 126).

Table 1 gives a summary of parameters for the models. For each NLFFF model, we computed a number of parameters: total poloidal flux, ratio of axial to poloidal flux, free energy (difference between the total magnetic energy and potential energy), and relative magnetic helicity.

The relative helicity computation method is described in Bobra et al. (2008, Appendix B). The NFR model poloidal and axial fluxes were kept the same as those of Model 126 in all 2FR system models. In the combined NFR + SFR system, we found that the SFR with reversed paths for both positive and negative signs of the poloidal flux was stable (Model 127) and marginally stable (Model 129), and also follows the helicity rule at high latitude.

The flux-rope insertion method preserves the axial flux but not the poloidal flux. Hence, the poloidal flux dissipates significantly in the process of MF relaxation. Therefore, the impact of reversing the poloidal flux sign has very little effect on the stability of the model. From here on, we use Model 126 and Model 127 as the most physically realistic of our best-fitting one-flux-rope and two-flux-rope stable models, respectively. The motivation to try models with a second flux rope in the southern cavity was that the direction of the spine from one flux rope did not match very well with the AIA observations, and we conjecture that adding currents, i.e., magnetic pressure in the form of a weakly twisted flux rope, in the other lobe would push the spine away back in the right direction to match better the AIA observations (these results are discussed further in the sections to follow.

The second to the last column of Table 1 quantifies helicity. The single-flux-rope case (126) results in a relative positive helicity of 12.4×10^{40} Mx^2. For the two stable flux ropes with reversed path and opposite signs of poloidal flux (case 127), there is less interconnectivity between the two flux ropes, i.e., less current sheet complexity, and the relative helicity is reduced to 3.95×10^{40} Mx^2. On the other hand, when we have two flux ropes with the same (regular) path directions and opposite signs of the poloidal flux (case 130), there is a transfer of flux between the two lobes of the pseudostreamer, hence more interconnectivity and relative helicity between the two flux ropes, and the helicity is increased to 19.2×10^{40} Mx^2. For the free energy, there are only slight differences between the single-flux-rope and the two-flux-rope cases, both with regular or reversed paths. From Table 1, we also notice that the change in the source-surface height (Models 126 versus 150 and 127 versus 151), which will be discussed later, has virtually no effect on the free energy and helicity.

Figure 4 shows top views of magnetic field lines from these two models. Figure 5 shows vertical cross sections through the flux ropes at the location of the yellow lines in Figure 4. A very sharp boundary is observed with two lobes and an X-point for both Models 126 and 127. Figures 6 and 7 show a variety of 3D views of the two models.

4. Analysis of the Magnetic Field and Topology

We analyzed the magnetic structure of the pseudostreamer using a map of squashing factors, Q (Titov 2007). Q is computed by grouping field lines into separate bundles, which connect disparate regions on the solar surface, and following their deviations as they pass between domains. These domains are bound by separatrices or quasi-separatrix layers (QSLs) in 3D (Priest & Démoulin 1995; Démoulin et al. 1996). QSLs are used as a proxy to determine where strong electric current sheets can develop in the corona and also to provide important information about the connectivity of complicated magnetic field configurations (Aulanier et al. 2005). Savcheva et al. (2012) performed the first topological analysis of an NLFFF magnetic field constrained by observations, demonstrating that topological analysis is extremely useful for pinpointing the probable sites of reconnection and finding the boundaries of the flux rope in an NLFFF model. Janvier et al. (2016) and Chintzoglou et al. (2017) showed that QSLs can accurately give the locations of magnetic nulls and separatrices.

Tassev & Savcheva (2017) introduced an open-source code for calculating Q in three dimensions—the `QSL squasher`, which is publicly available. The code takes as input any rectilinear sampling of a magnetic field in either spherical or Cartesian coordinates. The output can be a sampling of Q on a 3D grid, or on a planar or spherical slice.

Table 1
Representative Model Grid Parameters

Model	NFR ϕ_{axi} (10^{19} Mx)	NFR F_{pol} (10^9 Mx cm^{-1})	SFR ϕ_{axi} (10^{19} Mx)	SFR F_{pol} (10^9 Mx cm^{-1})	NFR T_{pol} (10^{20} Mx)	NFR (ϕ_{axi}/T_{pol})	SFR T_{pol} (10^{19} Mx)	SFR (ϕ_{axi}/T_{pol})	Free Energy (10^{30} erg)	Helicity (10^{40} Mx^2)	Stability
126	4	8	–	–	1.78	0.22	–	–	2.79	12.4	stable
127	4	8	2 (reversed path)	−1	1.78	0.22	−1.96	−1.02	3.14	3.95	stable
129	4	8	2 (reversed path)	1	1.78	0.22	1.96	1.02	3.16	4.05	marginally stable
128	4	8	2 (regular path)	1	1.78	0.22	1.96	1.02	3.08	19.2	unstable
130	4	8	2 (regular path)	−1	1.78	0.22	−1.96	−1.02	3.1	19.2	unstable
150	4	8	–	–	1.78	0.22	–	–	2.79	12.4	stable
151	4	8	2 (reversed path)	−1	1.78	0.22	−1.96	−1.02	3.14	3.99	stable

Note. Models 126, 127, 128, 129, and 130 are at 2.8 source-surface height while models 150 and 151 are at 2.5 source surface. The first column represents the model number. The second and third columns are the NFR axial and poloidal fluxes. The fourth column lists the SFR axial flux and also the direction of the SFR path. The fifth column lists the SFR poloidal flux. The total NFR and SFR poloidal fluxes are computed in the sixth and eighth columns. The ratio of axial to poloidal flux for both NFR and SFR are given in the seventh and ninth columns. Free energy and relative helicity are listed in the 10th and 11th columns respectively.

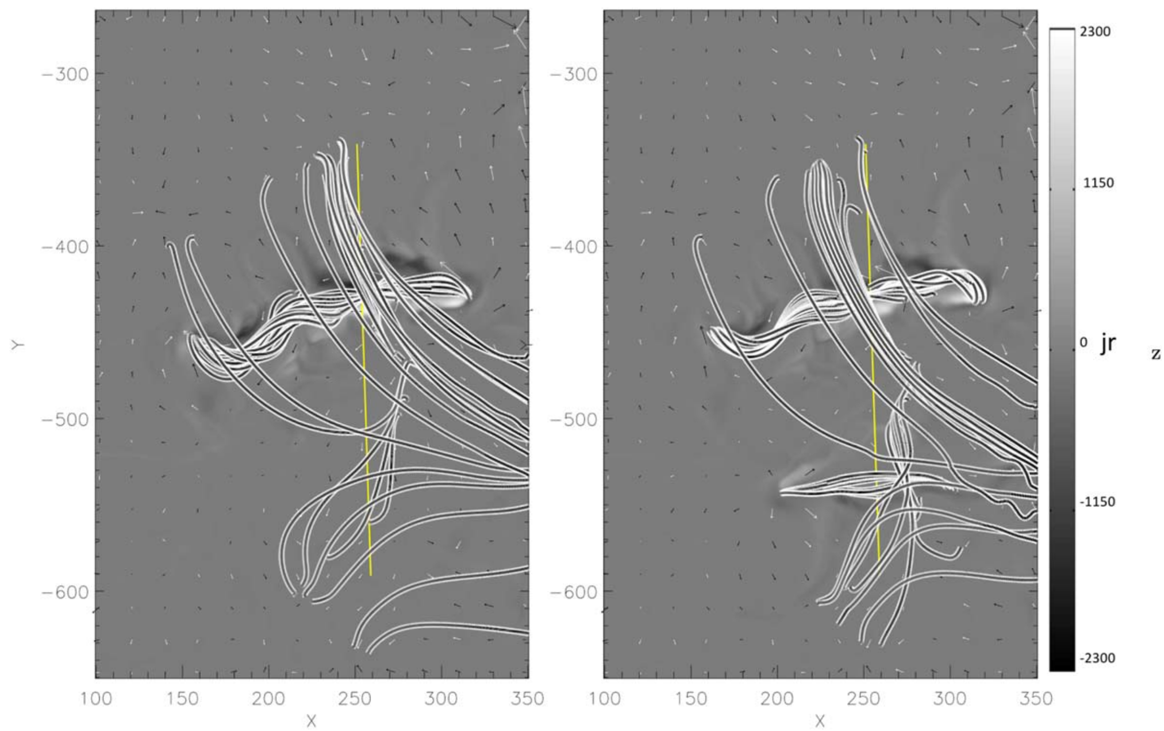

Figure 4. Best-fitting stable models of the pseudostreamer. Magnetic field lines are shown on a background of the radial component of the current density at 10 Mm height, $(j_r(x, y, 10))$. Arrows in the background are the vector magnetic field magnitudes. Left: Model 126 with only one flux rope inserted (NFR). Right: Model 127 with both NFR and SFR inserted.

We computed Q, the squashing factor, for entire volumes of our best-fitting models for both one- and two-flux-rope systems. Figure 8 shows that high-Q values are observed at the core of the cavity (yellow arrows), overlying arcade (red arrows), the fan (black arrows), the spine (white arrows), and 2D-projected magnetic null points (green arrows), which are the most probable sites for reconnection. The 2D cut (Figure 8) is rotated to match the time of CoMP observation. We identified the separatrix and its height and magnetic skeleton in 3D and its cross section with the given 2D cut exactly in our 3D code. This shows a typical pseudostreamer cavity configuration. From these pictures and with the tools implemented in the `QSL squasher` code, the position of the 2D-projected magnetic null point can be determined exactly. From these 2D slices, we can also confirm that both models are stable because there is a considerable distance between the flux arcade system and the fan; i.e., they do not touch.

5. Forward Modeling the Linear-polarization Signal

As discussed above, linear-polarization observations are ideally suited for probing certain topological properties of the coronal magnetic field. These include apparent magnetic null heights in pseudostreamers and also the expansion of open magnetic flux tubes, which we now discuss.

5.1. Coronal Apparent Magnetic Null Height from the Linear-polarization Fraction

As mentioned in Section 2, the linear-polarization measurements in the Fe XIII coronal line are subject to the van Vleck effect, i.e., a geometrically induced extinction of the polarization signal when the angle between the local vector magnetic field and radial direction is $\theta_B = 54\overset{\circ}{.}74$. Rachmeler et al. (2012) predicted that a magnetic null-point topology would produce a linear-polarization signal presenting four (more or less broad) van Vleck extinction lines converging into a single point (we refer to this as the “apparent magnetic null point”) and separating three polarization lobes. They showed that the convergence of the loci of the van Vleck angles, i.e., the apparent magnetic null point, could be used as a proxy of the true magnetic null-point location.

Gibson et al. (2017) demonstrated this diagnostic capability using CoMP observations. Following these authors’ approach, we examined images of forward modeled linear-polarization fractions to estimate the apparent magnetic null-point height by identifying the convergence of the polarization lobes (yellow stars in Figure 11). To compute the apparent magnetic null-point height, we built a small interactive program that returns the position of the apparent null based on clicking on the position of the loci of the van Vleck angles as seen by the user in images of the linear-polarization fraction. For a given linear-polarization fraction image, we perform several clicks at different positions where the loci of the van Vleck angles seems to be, which allows us to produce a mean and standard deviation of the likely position of the apparent magnetic null point that takes into account uncertainties related to the fact that the loci of the van Vleck angles are not always well defined. The resulting mean height and standard deviation values are reported in Table 2 and discussed in Section 5.3.2.

For both CoMP observations and the synthetic data from the models, we used the LoS-integrated linear-polarization fraction to estimate the apparent magnetic null heights. Thus, as is the case with the linear-polarization expansion factor that we will discuss in Sections 5.2 and 5.3.3, the comparison of observations to forward modeled quantities are equivalent. Nevertheless, it should be kept in mind that both have an LoS

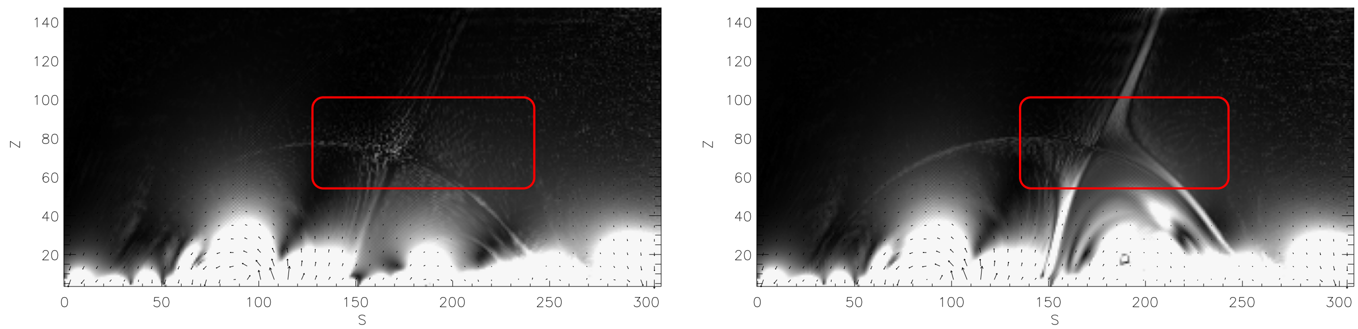

Figure 5. Distribution of the current density in a vertical cross section of the flux rope. The location of the vertical plane is shown by the yellow lines in Figure 4. Left: single flux rope (NFR) Model 126. Right: two flux ropes (NFR and SFR) Model 127. Arrows in the background are the vector magnetic field magnitudes. The 2D-projected magnetic null point (inside the red box), which is in fact a generalized X-line, or a hyperbolic flux tube (Titov 2007), is distorted in the horizontal direction. This distortion predisposes the magnetic structure for easier reconnection.

integration effect that separate them from the true magnetic quantity (magnetic null height and expansion factor).

5.2. Coronal Magnetic Expansion from Linear-polarization Azimuth

Coronal magnetic expansion is usually quantified through the calculation of a magnetic expansion factor. The magnetic expansion factor measures the degree of expansion (and contraction) of the cross section of magnetic flux tubes in the solar corona compared with their cross section at the solar photosphere. When the direction of the magnetic field, but not its strength, is known, the magnetic expansion factor can be defined as (e.g., Wang & Sheeley 1990)

$$f(\boldsymbol{r}, \Phi) = \frac{\mathcal{S}(\boldsymbol{r}, \Phi)}{\mathcal{S}(\boldsymbol{R}_\odot, \Phi)} \cdot \frac{R_\odot^2}{r^2}, \tag{3}$$

where $\mathcal{S}(\boldsymbol{r}, \Phi)$ is the cross-sectional area of a tube carrying magnetic flux, Φ, at position, $\boldsymbol{r}$, along its axis, $R_\odot$ is the solar radius, and $R_\odot^2/r^2$ is a correction factor accounting for the natural expansion of surfaces as r increases in spherical geometry (referred to as "radial expansion"). Then, the cross-sectional area of a magnetic flux tube, $\mathcal{S}(\boldsymbol{r}, \Phi)$, and the expansion factor, $f(\boldsymbol{r}, \Phi)$, can be computed by tracing closely spaced magnetic field lines and quantifying the deviations between them, similar to the calculations of the squashing factor used to identify QSLs (see Section 4).

CoMP coronal polarization data provide us with an effectively 2D PoS azimuth angle. This pseudo PoS azimuth further defines an effectively 2D PoS, normalized, vector magnetic field. Such data can thus be used to probe the expansion of the magnetic field in the solar corona. However, such a linear-polarization expansion factor (LPF) can only be a proxy of the true expansion factor of the coronal magnetic field. Furthermore, tracing field lines from such a 2D pseudo-vector magnetic field only provides us with 1D information on the cross-sectional area, $\mathcal{S}(\boldsymbol{r}, \Phi)$. As a consequence, there is no unique way to compute the LPF from CoMP data, and Gibson et al. (2017) introduced three different expressions including one for 3D flux tubes with a circular cross section, one for 2.5D flux tubes associated with an axisymmetric Sun, and one for 2.5D flux tubes with invariance in the LoS direction. For the cases presented in this paper, we compared all three LPF proxies and found that they are very similar in structure, despite the fact that they vary somewhat in magnitude. Our conclusions made by comparing the LPF measured from CoMP and our magnetic models are independent of which proxy is used. In this paper, we thus choose to use the Gibson et al. (2017) LPF proxy for 3D flux tubes with a circular cross section,

$$f^{(3\mathrm{D})}(\boldsymbol{r}(s)) = \left(\frac{\|\delta\boldsymbol{r}_\perp(s)\|}{\|\delta\boldsymbol{r}_\perp(s_\odot)\|}\right)^2 \cdot \frac{R_\odot^2}{r^2}, \tag{4}$$

where $\delta\boldsymbol{r}_\perp$ is the component of the field-line deviation perpendicular to the field line. $\delta\boldsymbol{r}_\perp(s)$ effectively represents the diameter of a 3D flux tube with a circular cross section, at position $\boldsymbol{r}(s)$ along the flux-tube axis with s corresponding to the curvilinear abscissa along it. $(r(s), \theta(s), \phi(s))$ are the spherical coordinates of the flux-tube axis. We use a predictor-corrector Euler algorithm and bilinear interpolation to integrate the polarization field lines and their field-line deviations $(\delta\boldsymbol{r}_\perp(s))$, following the azimuth down to the lower CoMP occulter.

5.3. Results

Using the FORWARD (Gibson et al. 2016) SolarSoft package, we compared synthetic observations generated from our NLFFF models to CoMP observables. In order to investigate the effect of adding currents, we also compared our synthetic NLFFF observables to synthetic PFSS observables as in Gibson et al. (2017). Figures 9 and 10 shows the full range of the different scenarios of the PFSS and NLFFF models that we compared. Note that the CMS PFSS and CMS NLFFF BCs differ by the flux sources added at the footprints of the FRs.

The LoS plasma weighting was obtained by defining density radial profiles consistent with hydrostatic equilibria in streamers versus coronal holes, and assigning these to closed versus open magnetic fields in the models, as discussed in Gibson et al. (2017). The parameters of these two hydrostatic equilibria were chosen such that the Fe XIII (1074.7 nm) integrated total line intensities (hereafter Stokes I) generated from our 3D magnetic models are similar to those measured by CoMP. For the PFSS model used in Gibson et al. (2017, hereafter the DeRosa PFSS), the plasma density at the coronal base was thus set to 5×10^8 cm^{-3} (10^8 cm^{-3}) for the closed (open) magnetic field, while the isothermal temperature was set to 1.5×10^6 K (10^6 K) for the closed (open) magnetic field. For all CMS models, we used the same parameters as those of the DeRosa PFSS for the closed magnetic field. All CMS models considered in this paper are 3D magnetic field models

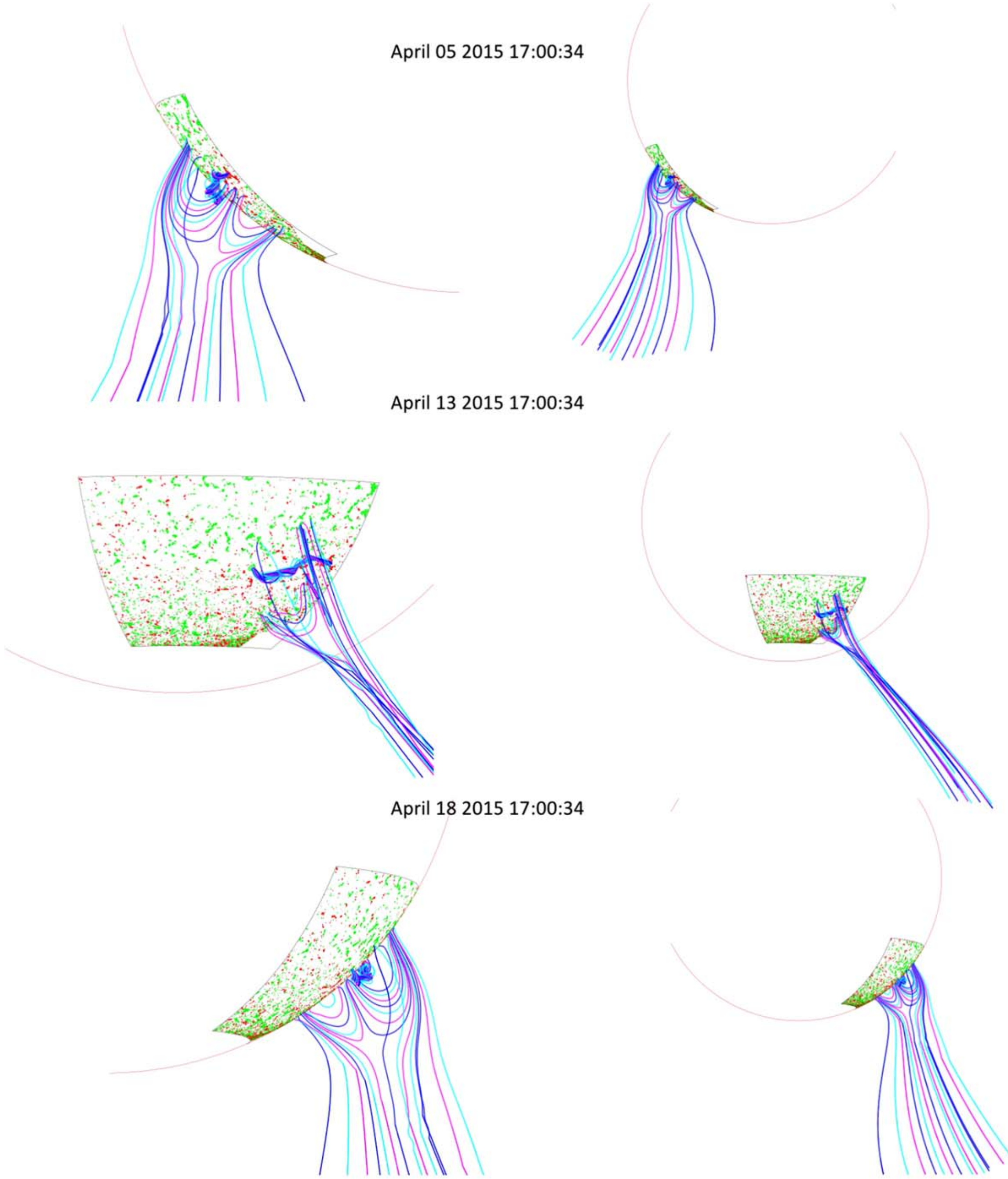

Figure 6. 3D views of Model 126: the pseudostreamer with only one flux rope inserted. Top panel: pseudostreamer at the southwestern limb rotated 180° degree in longitude to the east limb. Middle panel: rotated 90° in longitude to roughly central meridian. Bottom panel: pseudostreamer at the southeastern limb as seen from Earth.

in a spherical wedge, as opposed to the DeRosa PFSS, which is a global 3D model. For the forward calculations, we considered that there is no plasma outside of the CMS spherical wedge. Hence, in order to match the Stokes *I* from CoMP, the plasma parameters for the open magnetic field of the CMS models had to be set to values different from those of the DeRosa PFSS model. In particular, the open field of each CMS model has a plasma density at the coronal base set to 3×10^8 cm^{-3} and an associated isothermal temperature of 1.5×10^6 K.

We compared PFSS results at two source surface heights (denoted by "ss") and used two different boundary conditions: a PFSS model computed for a high-resolution subdomain embedded in a global magnetic synoptic map, which is denoted "embedded boundary" (EB), in which the field normal to the side boundaries must match the external field normal component, and a PFSS model computed only within the subdomain with no global map, denoted "open boundary" (OB), in which the field normal to the side boundaries expands freely outwards. The EB condition is achieved by using a standard web-served HMI synoptic map. The DeRosa synoptic map was generated by assimilating magnetograms into a flux transport model that evolves the magnetic field on the unobserved portions of the Sun with known differential rotation, meridional flow, and supergranular random walk (Schrijver & De

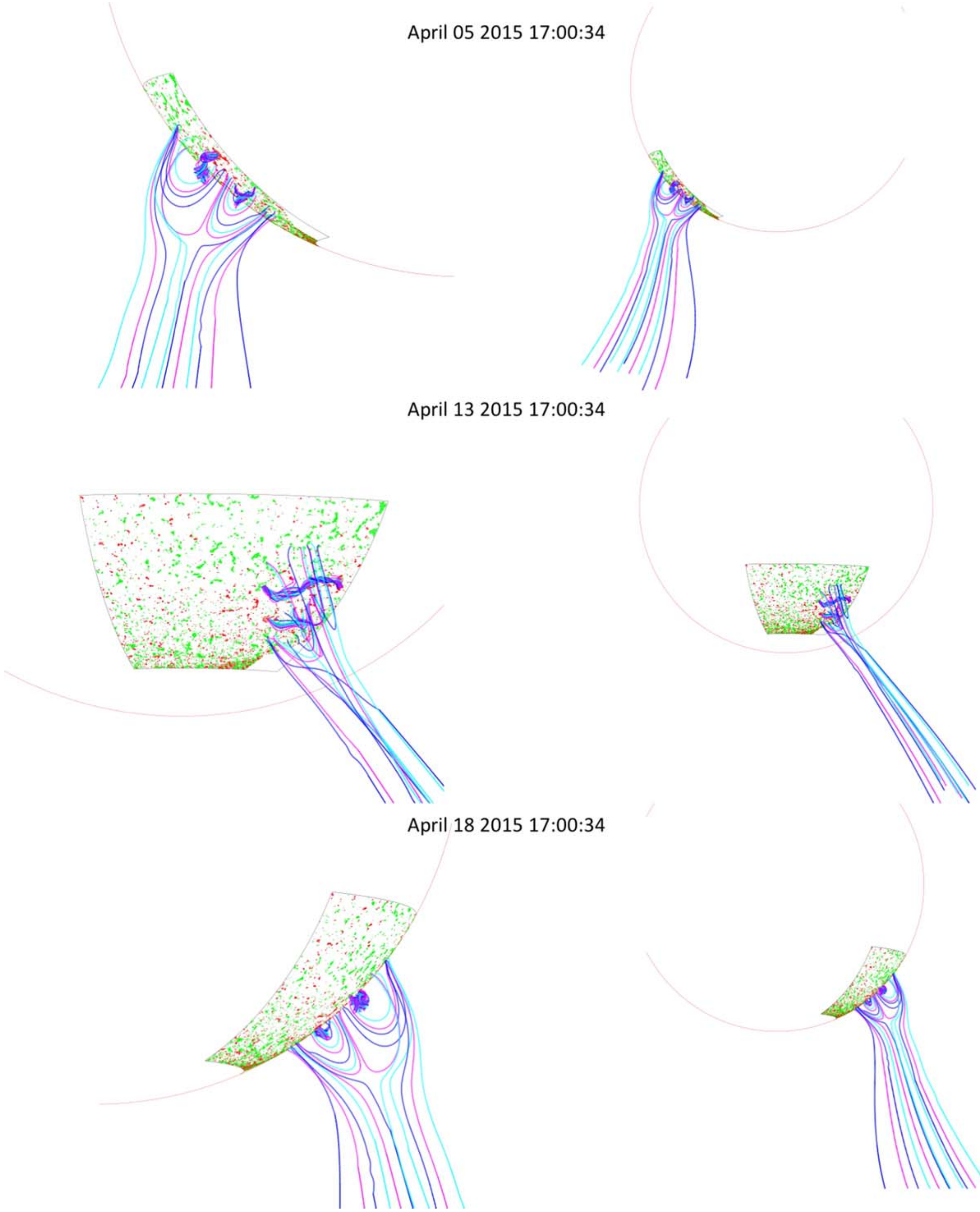

Figure 7. 3D views of Model 127: the pseudostreamer with two flux ropes inserted. Top panel: pseudostreamer at the southwestern limb rotated 180° degree in longitude to the east limb. Middle panel: rotated 90° in longitude to roughly central meridian. Bottom panel: pseudostreamer at the southeastern limb as seen from Earth.

Rosa 2003), whereas the HMI synoptic map is generated by concatenating near central-meridian 720 s LoS magnetograms onto the Carrington (latitude, longitude) frame over the course of the given Carrington Rotation (CR 2162). We computed NLFFF models at two source-surface heights for the OB conditions: 2.5 $R_\odot$ and 2.8 $R_\odot$ (Figure 10). We tested all of the cases shown in Figures 9 and 10, and show some illustrative examples in Figure 11.

We note that the spines of the modeled pseudostreamers were generally tilted more southward than the AIA observations (Figures 1(a) and (b)). Moreover, as we will further discuss in Section 5.3.1, in linear polarization, the 1FR system's southern lobe looked squeezed in comparison to the CoMP observations, Figure 11. Our motivation for trying two flux ropes was to inflate the southern lobe and push the spine northward. However, the inserted SFR neither helped to correct the inflation nor shifted the spine toward the north—i.e., the result was the same as for the 1FR system. We also tested if our bounding box was large enough to include the effects of the southern coronal hole, which may push the pseudostreamer

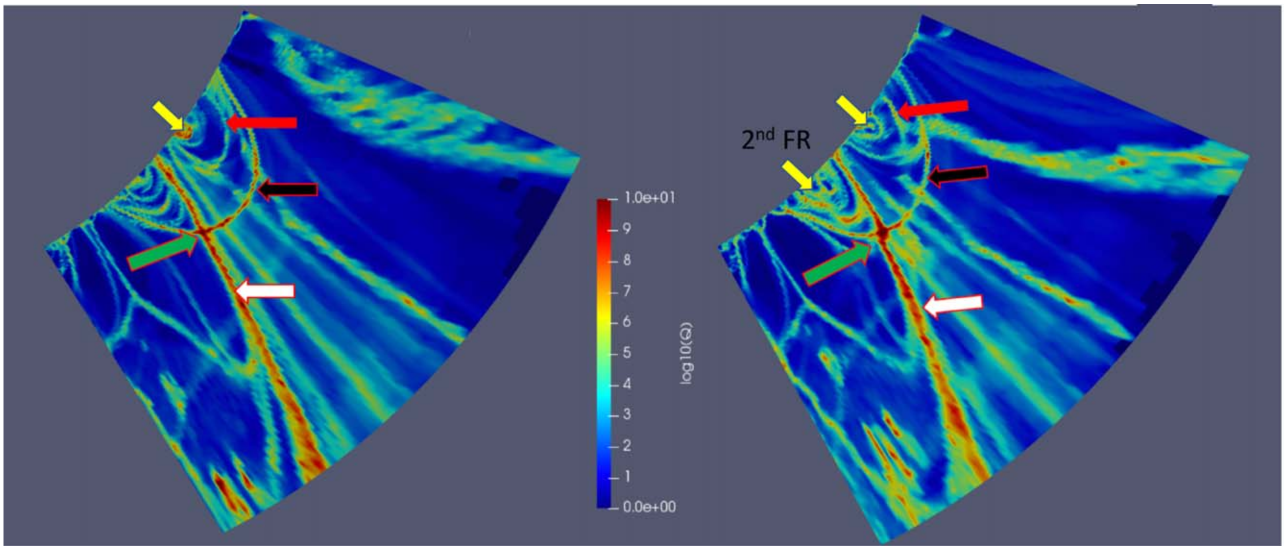

Figure 8. 2D slice of log10 Q for the one-flux-rope Model 126 (left) and the two-flux-rope Model 127 (right). Yellow, red, black, green, and white arrows point out the flux rope, the overlying arcade, fan, the 2D-projected magnetic null points, and the spines, respectively.

Table 2
Apparent Magnetic Null Point Heights.

Model	Apparent Magnetic Null Height ($R_\odot$)
CoMP	1.16 ± 0.012
DeRosa PFSS (2.5)	1.09 ± 0.007
CMS PFSS HMI low (EB) (2.5)	1.09 ± 0.005
CMS PFSS low (OB) (2.5)	1.11 ± 0.005
CMS PFSS high (OB) (2.8)	1.11 ± 0.005
Model 126 (1FR, 2.8)	1.17 ± 0.007
Model 127 (2FR, 2.8)	1.18 ± 0.006
Model 150 (1FR, 2.5)	1.17 ± 0.006
Model 151 (2FR, 2.5)	1.18 ± 0.007

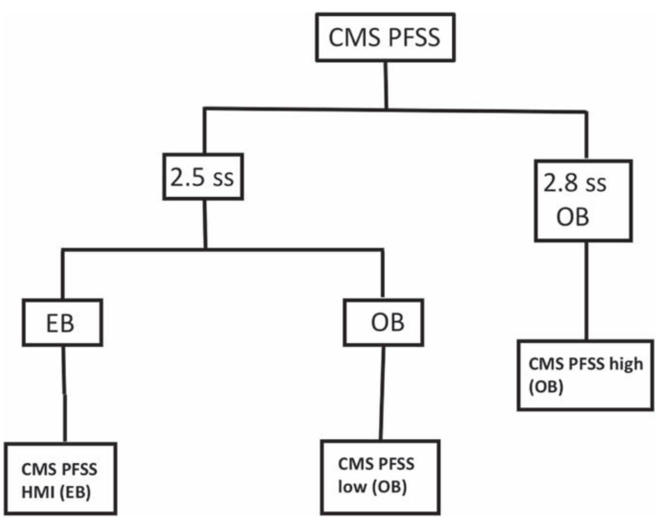

Figure 9. Different CMS PFSS models. OB and EB stand for open boundary (no global magnetic synoptic map used) and embedded boundary (global magnetic synoptic map used to define side boundaries), respectively. The EB condition is achieved using an HMI synoptic map. "ss" is source surface.

equatorward. To this end, we extended our box boundary farther south in latitude toward the pole and created two additional models having the same axial and poloidal fluxes as our best-fit 1FR and 2FR models, respectively. However, no change in the spine tilt was observed. It is possible that (a) an HMI magnetogram is too noisy at the poles and does not provide a reliable magnetic field at the poles or (b) dynamic pressure from the fast solar wind coming from the southern coronal hole is not included in our model (because it is not fully MHD), which might contribute to bending the spine equatorward.

5.3.1. Linear-polarization Fraction

Figure 11 presents the linear-polarization fraction synthesized for all our magnetic models in comparison with CoMP data. For all PFSS models, we find van Vleck extinction lines converging into a single point (the apparent magnetic null point) and separating three polarization lobes forming a dome-like structure, which is a typical polarization signature for magnetic null-point topologies (see Section 5.1). Despite these similarities, Figure 11 also shows significant differences between the linear-polarization signals synthesized from the DeRosa PFSS and the CMS PFSS models (EB and OB). In particular, the northern lobe of the DeRosa PFSS is bigger and more bulged than in any of the CMS PFSS models. The difference between the DeRosa PFSS and the CMS PFSS models is likely due to differences in the assumed underlying photospheric boundary condition. The DeRosa PFSS is a global extrapolation that uses data assimilation and flux transport to specify the full-Sun magnetic field, whereas the CMS PFSS models are produced at higher spatial resolution from individual HMI photospheric magnetograms at their lower boundary.

This higher resolution is necessary to resolve the width of the flux rope to be inserted into the CMS PFSS solution when generating the (CMS) NLFFF model. In addition, we notice that the three lobes are slightly smaller in the CMS PFSS HMI Low (EB) than in the CMS PFSS Low (OB). This is likely due to the difference in the side boundary conditions (see discussion at the end of the introduction of Section 5.3).

The three lobe structures in the linear polarization possess larger cross sections and are more bulged and elevated in the synthetic data produced from the NLFFF models. We also find that, while being relatively similar, the van Vleck extinction lines are different enough for NLFFF 1FR (Model 150)

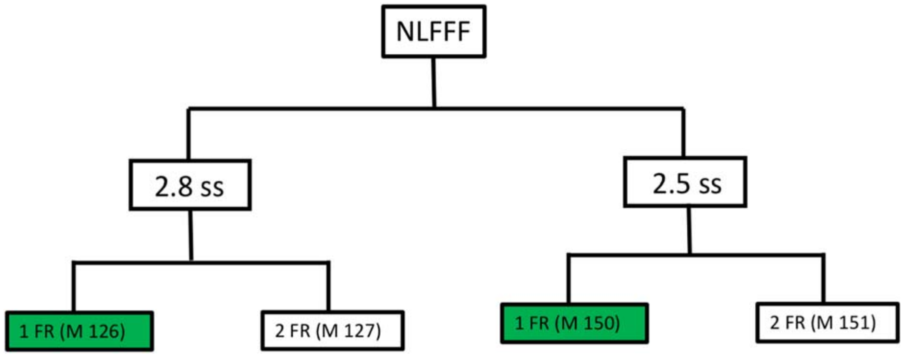

Figure 10. Different NLFFF models. 1FR and 2FR denote the number of flux ropes inserted. NLFFF models are generated without global synoptic maps (OB). "ss" is source surface. Green represents the best models.

compared with NLFFF 2FR (Model 151) to distinguish between the two models. In particular, the two southern extinction lines, which are in the region where the second flux rope was inserted, are significantly fainter for NLFFF 2FR (Model 151).

Comparing the results obtained from CMS PFSS Low (OB), NLFFF 1FR (Model 150), and NLFFF 2FR (Model 151) with the results obtained from their counterpart CMS PFSS High (OB), NLFFF 1FR (Model 126), and NLFFF 2FR (Model 127) further allows us to investigate the effect of moving the source-surface height from $2.5R_{\odot}$ (for the former three models) to $2.8R_{\odot}$ (for the latter three models) on our calculations of the linear-polarization fraction. For the tests considered here, we find that the three-lobe patterns in the linear polarization remain unaffected by the change of source-surface height (see Figure 11).

Finally, we compare the polarization signal from all of our 3D magnetic field models to CoMP observations. In agreement with the results of Gibson et al. (2017), we find that all PFSS models considered are not able to fully capture the bulging nature of the northward lobe observed with CoMP. Only our NLFFF models provide the best qualitative match to the linear-polarization fraction measured by CoMP. Our results therefore suggest the presence of at least one strong and concentrated electric current channel below the pseudostreamer.

5.3.2. Apparent Magnetic Null Point Height

Figure 11 shows that the apparent magnetic null point (i.e., the loci of the van Vleck extinction lines) is somewhat to the left of the center of the dome in all considered PFSS models and roughly at the same height. This is confirmed by the quantitative analysis reported in Table 2 and derived from the procedure described at the end of Section 5.1. In particular, we find that the apparent magnetic null height is $\approx 1.09R_{\odot}$ for both the DeRosa PFSS and the CMS PFSS HMI Low (EB) models, while it is $\approx 1.11R_{\odot}$ for CMS PFSS Low (OB).

As with the PFSS models, the apparent magnetic null point is found slightly to the left of the center of the dome for all NLFFF models. However, the flux-rope cases all produce a polarization signal in which the apparent magnetic null point is at a much higher altitude than in the PFSS models. We further notice that the two-flux-rope model (NLFFF 2FR Models 127, 151) results in an apparent magnetic null point of $\approx 1.18R_{\odot}$, which is slightly higher than the $\approx 1.17R_{\odot}$ obtained with the single-flux-rope model (NLFFF 1FR Models 126, 150). As is generally true for the linear-polarization signal (cf. Section 5.3.1), we find that the apparent magnetic null-point height remains unaffected by the change of source-surface height (see Table 2).

The comparison with CoMP data, in which the apparent magnetic null height is $\approx 1.16R_{\odot}$, reveals that all of our PFSS models systematically underestimate the altitude of the apparent magnetic null point, thus confirming the findings of Gibson et al. (2017). For the set of magnetic field models considered, we find that the models containing a single flux rope below the northern lobe of the pseudostreamer (NLFFF 1FR Models 126, 150) provide us with the best match to the apparent magnetic null height seen in CoMP observations. Our results thus argue in favor of a single strong electric current channel lying in the northern lobe below the pseudostreamer.

5.3.3. Linear-polarization Expansion Factor

Figure 12 displays the LPF and selected linear-polarization field lines derived from the linear-polarization signal observed by CoMP and those synthesized for all our magnetic models. When the angle between the local magnetic vector and radial direction becomes larger than the van Vleck angle, the direction of the linear-polarization vector, i.e., the azimuth, is rotated by 90° (e.g., Judge 2007). As a consequence, linear-polarization field lines may cross the van Vleck extinctions lines, in which case their corresponding LPF calculations are unusable. To avoid such ambiguous regions where the van Vleck extinction lines are crossed, the results of our LPF calculations are only shown and analyzed for the zoomed in region that lies on the northern part of the pseudostreamer (and indicated by a red rectangle in Figure 11), as it was in Gibson et al. (2017). We note, though, that the bottom-left corner of the FOV shown in Figure 12 and dominated by subradial expansion for both CoMP and our magnetic models actually corresponds to one of those ambiguous regions, which is why we disregard it in our analysis.

Apart from a small region on the top-right corner where both the DeRosa PFSS and CMS PFSS HMI Low (EB) show some weak subradial expansion, we find that all of the considered PFSS models display super-radial expansion in the analyzed FOV. The LPF from our CMS PFSS HMI Low (EB) model generally agrees with the LPF derived from the DeRosa PFSS, despite the differences in the photospheric boundary condition discussed in Section 5.3.1. However, we find that the CMS PFSS Low/High (OB) exhibit a much stronger super-radial expansion than the other two PFSS models, as further confirmed by the shape and radial divergence of the overplotted linear-polarization field lines (green lines in Figure 12). This difference with the LPF calculations from the DeRosa PFSS

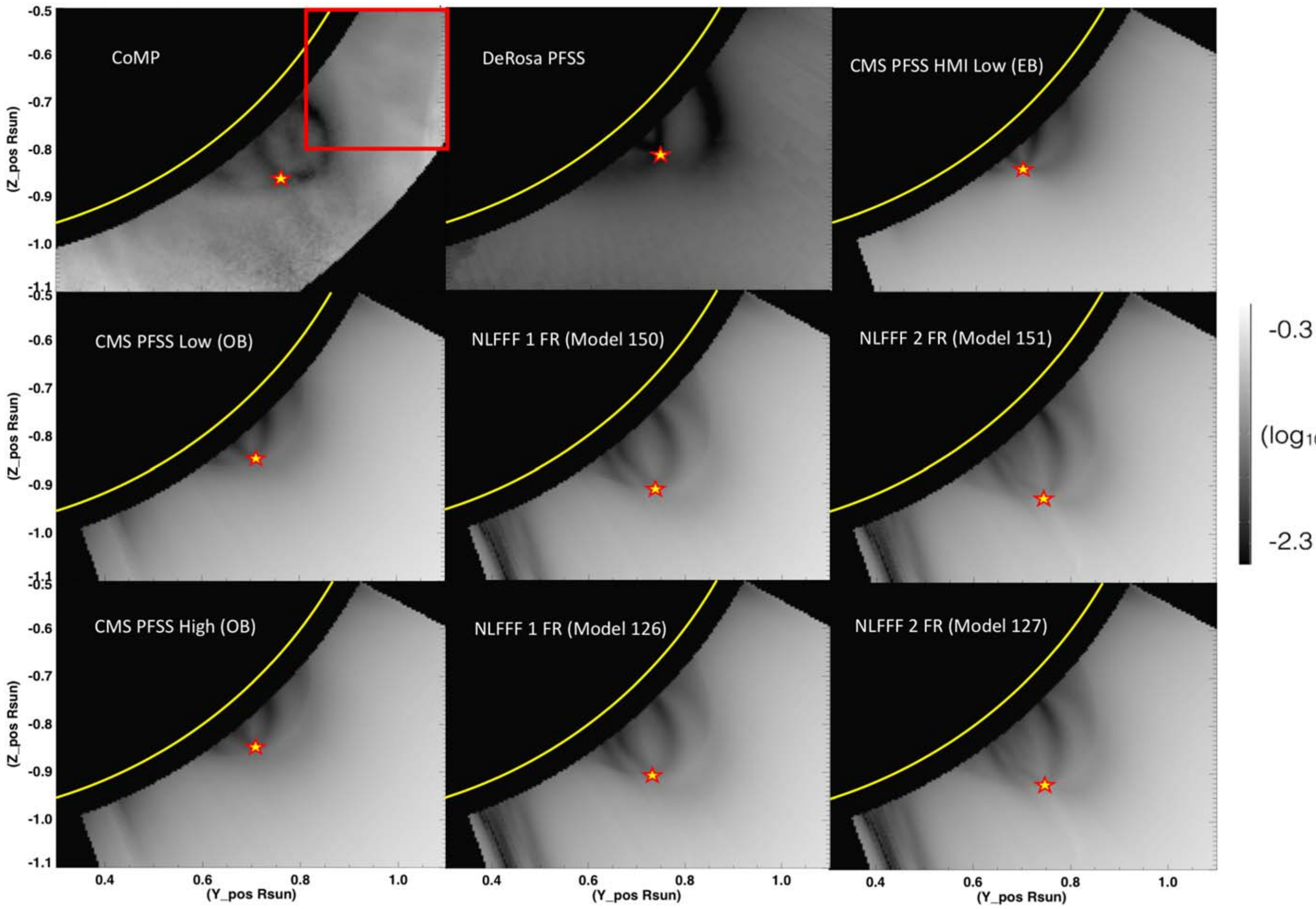

Figure 11. Comparison of the linear-polarization fraction (L/I) of the CoMP observations with the synthetic data generated from our PFSS and NLFFF models (described in Sections 3.2 and 3.3). First row: synthetic linear-polarization magnitude (L/I) images of the CoMP observation, DeRosa PFSS model corresponding to the one used in the Gibson et al. (2017) paper, and CMS PFSS model computed using photospheric boundary and embedded side boundaries as described in the text. The red rectangular box plotted over the CoMP L/I image highlights the zoomed in region analyzed in Figure 12. Second row: L/I images of the CMS PFSS model computed without using the global synoptic map (open side boundary) as described in the text, and NLFFF one-flux-rope model and NLFFF two-flux-rope model (both with open side boundaries). First and second row models were computed at 2.5 source surfaces. Third row: L/I images computed at 2.8 source surface of the CMS PFSS model computed without using the global synoptic map (open side boundary), and NLFFF one-flux-rope model and NLFFF two-flux-rope model (both with open boundaries).

and CMS PFSS HMI Low (EB) models is likely due to the fact that CMS PFSS Low/High (OB) models are only computed for the photospheric sub-ROI without embedding in a global synoptic map (as opposed to the other two PFSS solutions) and with the field normal to the side boundaries allowed to expand freely outwards (see the related discussion in the introduction of Section 5.3).

The LPF calculations from our NLFFF models display strong super-radial expansion. The LPF and linear-polarization field lines computed from NLFFF 1FR (Models 126/150) and NLFFF 2FR (Models 127/151) cannot, however, be distinguished. This is likely because the second flux rope in the two-flux-rope models (NLFFF 2FR Model 127/151) is in the southern part of the pseudostreamer and is not strong enough to significantly alter the 3D magnetic field, and the resulting polarization signal, in the northern part of the pseudostreamer. Indeed, the linear-polarization fraction of the two-flux-rope models only significantly differs from that of the single-flux-rope model in the southern part of the pseudostreamer, i.e., where the second flux rope lies in NLFFF 2FR (Models 127/151; see Figure 11). For the LPF and linear-polarization field lines, we find that the results are not modified by the change of source-surface height (see Figure 12).

Overall, we find that all of our NLFFF models provide a much better match to the CoMP LPF than the DeRosa PFSS and CMS PFSS HMI Low (EB), both of which clearly underestimate the super-radial expansion exhibited by CoMP measurements. However, and for the considered FOV only, the LPF calculated from the CMS PFSS Low (OB) models captures the CoMP LPF similarly well and is almost indiscernible from the LPF computed with our NLFFF models, which we note, again, also have open boundaries.

Interpreting the significance of these differences and in comparison to CoMP data is somewhat difficult. It is possible that the increased lateral expansion that is a consequence of the open side boundaries in the CMS PFSS Low (OB) models is mimicking the effect of coronal currents on the magnetic field expansion. Alternatively, it could mean that the global PFSS synoptic boundary condition, which becomes less accurate at the limb, is overconfining the pseudostreamer fields in the DeRosa and CMS PFSS HMI Low (EB) models. The Gibson et al. (2017) conclusion is not supported in these experiments, but more investigation is required. Furthermore, it shows that the LPF calculations may not be a good discriminator of 3D magnetic field models without additional observational constraints (e.g., instantaneous 4π sr photospheric magnetograms).

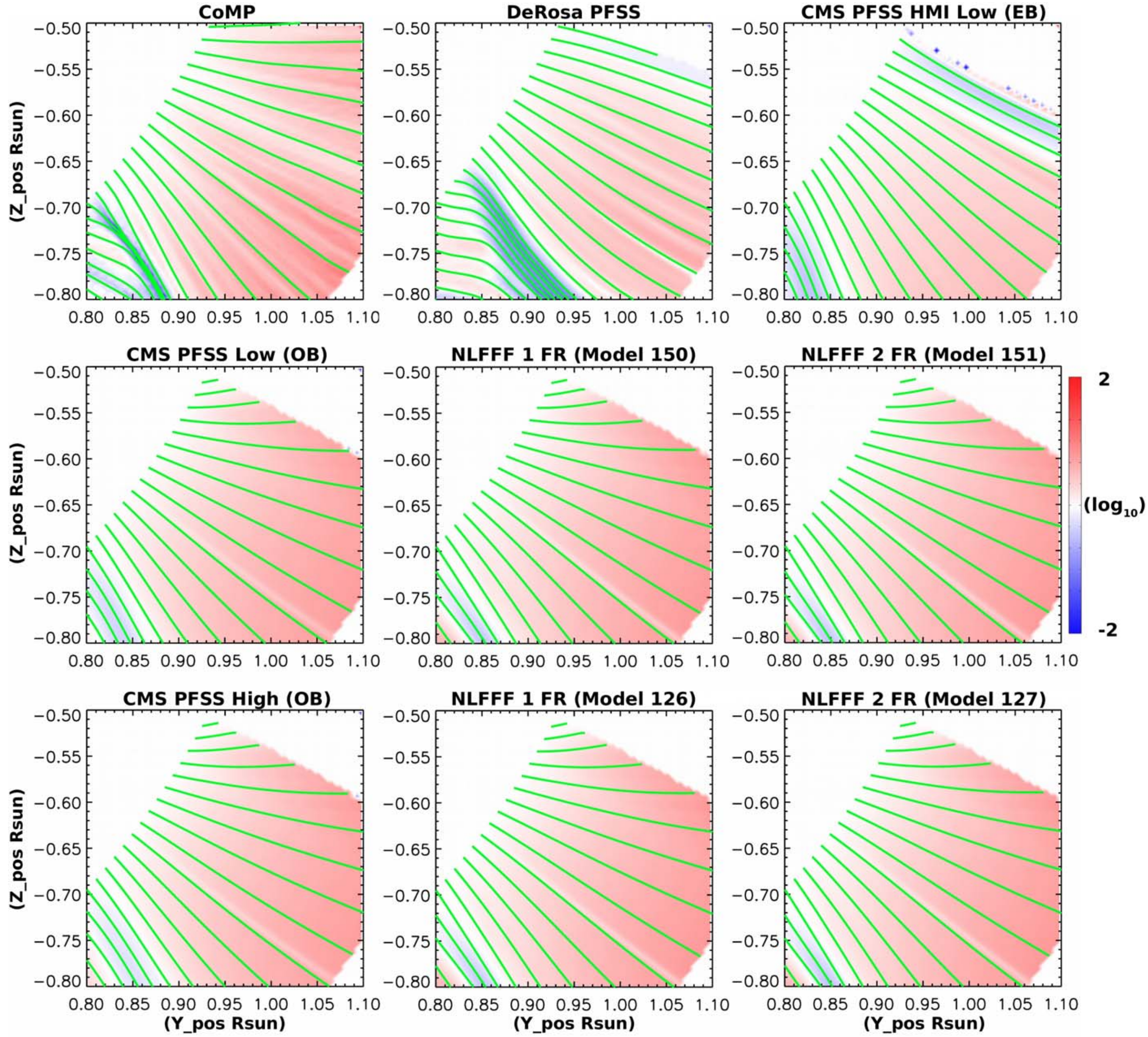

Figure 12. Zoom-in of the upper-right region of the pseudostreamer shown in Figure 11. Top left: LPF calculated for CoMP. Other panels show results for models as in Figure 11. Polarization field lines are plotted on top of LPF, with color scaling indicating radial expansion (white), super-radial expansion (red), subradial expansion (blue)).

6. Conclusion and Discussion

We presented a magnetic field configuration of a pseudostreamer embedding a cavity using an NLFFF flux-rope insertion model. We studied how the axial and poloidal fluxes, length of flux rope, source surface, and wedge size impacted the stability of the NLFFF models. We also performed a topological analysis of the models in order to determine the locations of QSLs. Further, we used FORWARD to produce synthetic observables from both the NLFFF flux-rope and potential-field (PFSS) models, and compared these to CoMP observations to determine the apparent magnetic null height and open field expansion factor. Our major results are summarized as follows:

1. We considered multiple options for flux-rope length, insertion height, axial flux, as well as number of flux ropes (one versus two) and sign of helicity (see Figure 3). We found four stable solutions that also followed the helicity rule for high latitudes: the single-FR Model 126, the double-FR Model 127, and the two equivalent Models 150 and 151, which had lower source surfaces (see Table 1). We found all of these models gave almost similar results in terms of the magnetic morphology and topology, with a magnetic null point or line clearly visible in the Q-maps (Figure 8).
2. Apparent magnetic nulls forward modeled in linear polarization from the best-fit NLFFF models appeared in the regions of the Q-map 2D-projected magnetic nulls, as expected, and we determined these heights through visual inspection, with error bars representing the uncertainty in the measurement (Table 2).

3. Inserting one or two flux ropes resulted in the elevation of the forward modeled apparent magnetic null point. Among all models, the single-flux-rope models were the ones that resulted in an apparent magnetic null-point height comparable to the one observed in CoMP linear polarization. Moreover, using AIA observations indicating a prominence and cavity only in the northern lobe of the pseudostreamer, we concluded that the single-flux-rope model (our models 126 and 150) was the best match to observations of the models that we considered.
4. For all of our NLFFF solutions, we used open side boundaries and an HMI LoS daily magnetogram. We created PFSS extrapolations from the HMI daily magnetogram both with open side boundaries and with side boundaries determined by embedding the wedge in global extrapolations of an HMI synoptic map, and compared these to the DeRosa PFSS extrapolation used in Gibson et al. (2017). We found differences between apparent magnetic null heights for these different PFSS models. However, unlike the NLFFF solution, all of the PFSS solutions predicted null heights lower than CoMP observations (Figure 11).
5. The linear-polarization expansion factor (LPF) and linear-polarization field-line calculations from our NLFFF models captured the magnetic expansion inferred from CoMP qualitatively well and better than some PFSS models. However, we found that the LPF calculations could not distinguish between our single- and two-FR models. We further found that other factors, like boundary conditions, could seriously impact the interpretation of the LPFs. In particular, we found that our open-boundary PFSS models matched the LPF inferred from CoMP as successfully as our NLFFF models. The initial conclusion of Gibson et al. (2017) that CoMP observations of LPF are inconsistent with PFSS models therefore needs to be reconsidered. On the other hand, we emphasize that the LPF calculations derived from CoMP polarization measurements provide us with a useful model-independent measure of the local, coronal magnetic expansion. However, for these LPF calculations to be successfully used to discriminate 3D magnetic field models, additional observational constraints will be required (such as instantaneous 4π sr photospheric magnetograms).

Because in the process of this modeling we extended our grid of models into the unstable range, it is now easy to explore the eruption of the cavity on April 19 that was observed well by AIA, SWAP, and LASCO. We will analyze the QSL evolution and eruption scenario. We leave this study for the follow-up paper.

The authors thank Adriaan van Ballegooijen, Yingna Su, and Laurel Rachmeler for helpful discussion. The AIA and HMI data are courtesy of NASA/*SDO* and the AIA and HMI Science Investigation Teams. CoMP data are provided courtesy of the Mauna Loa Solar Observatory, operated by the High Altitude Observatory (HAO), as part of the National Center for Atmospheric Research (NCAR). This material is based upon work supported by the National Center for Atmospheric Research, which is a major facility sponsored by the National Science Foundation under Cooperative Agreement No. 1852977. This work was supported by the Air Force Office of Scientific Research grant FA9550-15-1-0030, and in part by NASA grant NNX17AI27G. K.D. gratefully acknowledges the support of the French Centre National d'Études Spatiales.

ORCID iDs

Nishu Karna https://orcid.org/0000-0002-1314-4690
Antonia Savcheva https://orcid.org/0000-0002-5598-046X
Kévin Dalmasse https://orcid.org/0000-0001-8929-4006
Sarah Gibson https://orcid.org/0000-0001-9831-2640
Edward E. DeLuca https://orcid.org/0000-0001-7416-2895

References

Amari, T., Boulmezaoud, T. Z., & Aly, J. J. 2006, A&A, 446, 691
Amari, T., Boulmezaoud, T. Z., & Mikic, Z. 1999, A&A, 350, 1051
Asgari-Targhi, M., & van Ballegooijen, A. A. 2012, ApJ, 746, 81
Aulanier, G., Pariat, E., & Démoulin, P. 2005, A&A, 444, 961
Bąk-Stęślicka, U., Gibson, S. E., Fan, Y., et al. 2013, ApJ, 770, 28
Bhattacharjee, A., & Hameiri, E. 1986, PhRvL, 57, 206
Bobra, M. G., van Ballegooijen, A. A., & DeLuca, E. E. 2008, ApJ, 672, 1209
Boozer, A. H. 1986, JPlPh, 35, 133
Cheung, M. C. M., & DeRosa, M. L. 2012, ApJ, 757, 147
Chintzoglou, G., Vourlidas, A., Savcheva, A., et al. 2017, ApJ, 843, 93
Chodura, R., & Schlueter, A. 1981, JCoPh, 41, 68
Démoulin, P., Priest, E. R., & Lonie, D. P. 1996, JGR, 101, 7631
Dove, J. B., Gibson, S. E., Rachmeler, L. A., Tomczyk, S., & Judge, P. 2011, ApJL, 731, L1
Gibb, G. P. S., Mackay, D. H., Green, L. M., & Meyer, K. A. 2014, ApJ, 782, 71
Gibson, S., Kucera, T., White, S., et al. 2016, FrASS, 3, 8
Gibson, S. E., Dalmasse, K., Rachmeler, L. A., et al. 2017, ApJL, 840, L13
Grad, H., & Rubin, H. 1958, UN Int. Conf. on the Peaceful Uses of Atomic Energy in Theoretical and Experimental Aspects of Controlled Nuclear Fusion (Geneva: United Nations), 190, http://www.iaea.org/inis/collection/NCLCollectionStore/_Public/39/082/39082383.pdf?r=1
He, H., & Wang, H. 2008, JGRA, 113, A05S90
He, H., Wang, H., & Yan, Y. 2011, JGRA, 116, A01101
Hoeksema, J. T., Liu, Y., Hayashi, K., et al. 2014, SoPh, 289, 3483
Hundhausen, A. J. 1972, Coronal Expansion and Solar Wind (Berlin: Springer)
Inoue, S., Kusano, K., Magara, T., Shiota, D., & Yamamoto, T. T. 2011, ApJ, 738, 161
Inoue, S., Magara, T., Watari, S., & Choe, G. S. 2012, ApJ, 747, 65
Janvier, M., Savcheva, A., Pariat, E., et al. 2016, A&A, 591, A141
Jiang, C., & Feng, X. 2012, ApJ, 749, 135
Jiang, C., Feng, X., Fan, Y., & Xiang, C. 2011, ApJ, 727, 101
Judge, P. G. 2007, ApJ, 662, 677
Karna, N., Pesnell, W. D., & Zhang, J. 2015, ApJ, 810, 123
Lemen, J. R., Title, A. M., Akin, D. J., et al. 2012, SoPh, 275, 17
Lin, H., Kuhn, J. R., & Coulter, R. 2004, ApJL, 613, 177
Mackay, D., & Yeates, A. 2012, LRSP, 9, 6
Mackay, D. H., Green, L. M., & van Ballegooijen, A. 2011, ApJ, 729, 97
Malanushenko, A., Schrijver, C. J., DeRosa, M. L., Wheatland, M. S., & Gilchrist, S. A. 2012, ApJ, 756, 153
Mikic, Z., & McClymont, A. N. 1994, in ASP Conf. Ser. 68, Solar Active Region Evolution: Comparing Models with Observations, ed. K. S. Balasubramaniam & G. W. Simon (San Francisco, CA: ASP), 225
Parnell, C. E., Maclean, R. C., & Haynes, A. L. 2010, ApJL, 725, L214
Pesnell, W. D., Thompson, B. J., & Chamberlin, P. C. 2012, SoPh, 275, 3
Pevtsov, A. A., Balasubramaniam, K. S., & Rogers, J. W. 2003, ApJ, 595, 500
Priest, E. 2014, Magnetohydrodynamics of the Sun (Cambridge: Cambridge Univ. Press)
Priest, E. R., & Démoulin, P. 1995, JGR, 100, 23443
Rachmeler, L. A., Casini, R., & Gibson, S. E. 2012, in ASP Conf. Ser. 463, Second ATST-EAST Meeting: Magnetic Fields from the Photosphere to the Corona, ed. T. R. Rimmele et al. (San Francisco, CA: ASP), 227
Rachmeler, L. A., Gibson, S. E., Dove, J. B., DeVore, C. R., & Fan, Y. 2013, SoPh, 288, 617
Rachmeler, L. A., Platten, S. J., Bethge, C., Seaton, D. B., & Yeates, A. R. 2014, ApJL, 787, L3
Roumeliotis, G. 1996, ApJ, 473, 1095
Sakurai, T. 1981, SoPh, 69, 343
Savcheva, A., Pariat, E., McKillop, S., et al. 2016, ApJ, 817, 43

Savcheva, A., Pariat, E., van Ballegooijen, A., Aulanier, G., & DeLuca, E. 2012, ApJ, 750, 15
Savcheva, A., & van Ballegooijen, A. 2009, ApJ, 703, 1766
Savcheva, A., Van Ballegooijen, A. A., & DeLuca, E. E. 2012, ApJ, 744, SBD12
Schrijver, C. J., & De Rosa, M. L. 2003, SoPh, 212, 165
Su, Y., Surges, V., van Ballegooijen, A., DeLuca, E. E., & Golub, L. 2011, ApJ, 734, 53
Su, Y., & van Ballegooijen, A. 2012, ApJ, 757, 168
Su, Y., van Ballegooijen, A., Lites, B. W., et al. 2009, ApJ, 691, 105
Tassev, S., & Savcheva, A. 2017, ApJ, 840, 89
Titov, V. S. 2007, ApJ, 660, 863
Titov, V. S., Hornig, G., & Démoulin, P. 2002, JGRA, 107, 1164
Titov, V. S., Mikić, Z., Linker, J. A., Lionello, R., & Antiochos, S. K. 2011, ApJ, 731, 111
Titov, V. S., Mikic, Z., Török, T., Linker, J. A., & Panasenco, O. 2012, ApJ, 759, 70
Tomczyk, S., Card, G. L., Darnell, T., et al. 2008, SoPh, 247, 411
Valori, G., Kliem, B., & Fuhrmann, M. 2007, SoPh, 245, 263
Valori, G., Kliem, B., & Keppens, R. 2005, A&A, 433, 335
van Ballegooijen, A. A. 2004, ApJ, 612, 519
Velli, M., Lionello, R., Linker, J. A., & Mikić, Z. 2011, ApJ, 736, 32
Wang, Y.-M., Biersteker, J. B., Sheeley, N. R., Jr., et al. 2007a, ApJ, 660, 882
Wang, Y. M., & Sheeley, N. R. J. 1990, ApJ, 355, 726
Wang, Y.-M., Sheeley, N. R., Jr., & Rich, N. B. 2007b, ApJ, 658, 1340
Wheatland, M. S. 2004, SoPh, 222, 247
Wheatland, M. S. 2006, SoPh, 238, 29
Wheatland, M. S., Sturrock, P. A., & Roumeliotis, G. 2000, ApJ, 540, 1150
Wiegelmann, T. 2004, SoPh, 219, 87
Wiegelmann, T., Inhester, B., & Sakurai, T. 2006, SoPh, 233, 215
Wiegelmann, T., Neukirch, T., Ruan, P., & Inhester, B. 2007, A&A, 475, 701
Yan, Y., & Li, Z. 2006, ApJ, 638, 1162
Yan, Y., & Sakurai, T. 2000, SoPh, 195, 89
Yang, W. H., Sturrock, P. A., & Antiochos, S. K. 1986, ApJ, 309, 383
Zhao, X. P., & Webb, D. F. 2003, JGRA, 108, 1234